remote sensing

MDPI

Article

Analysis of the Ionospheric Irregularities and Phase Scintillation at Low and Middle Latitudes Based on Swarm Observations

Jiawei Kuai [1], Kang Wang [1], Jiahao Zhong [2,3,*], Xin Wan [2,3,4], Fuqing Huang [4,5], Hao Sun [1], Jiawen Chen [2], Xingyan Song [2] and Hao Han [2]

[1] College of Astronautics, Nanjing University of Aeronautics and Astronautics, Nanjing 210016, China
[2] Planetary Environmental and Astrobiological Research Laboratory (PEARL), School of Atmospheric Sciences, Sun Yat-sen University, Zhuhai 519082, China
[3] Key Laboratory of Tropical Atmosphere-Ocean System, Ministry of Education, Zhuhai 519082, China
[4] Mengcheng National Geophysical Observatory, University of Science and Technology of China, Hefei 230026, China
[5] CAS Key Laboratory of Geospace Environment, School of Earth and Space Sciences, University of Science and Technology of China, Hefei 230026, China
* Correspondence: zhongjh55@mail.sysu.edu.cn

Abstract: This study presents a statistical analysis of the ionospheric irregularities and topside ionospheric scintillation at low and middle latitudes by using in situ electron density and upward-looking total electron content data measured by the Swarm constellation during 2014–2021. The main purpose of this study is to determine whether the phase scintillation could present similar seasonal, longitudinal, latitudinal, local time, and solar activity features as the in situ ionospheric irregularities do at low and middle latitudes, and how the irregularities affect the phase scintillation. The results are summarized as follows: (1) At low latitudes, the occurrence rate of equatorial plasma irregularities (EPIs) at the equinoxes and December solstice peaks before midnight, but during the June solstice, the EPIs mainly occur after midnight. The occurrence rate of EPIs has a positive correlation with solar activity. The distribution of topside scintillation occurrence is relatively consistent with EPIs, but during the June solstice, the scintillation occurrence rate remains at a very low level. (2) The midlatitude irregularities mainly occur after midnight, and their occurrence rate is negatively correlated with solar activity. Midlatitude irregularities mainly occur during the solstices, concentrated over the Pacific region during the June solstice and over the Pacific American sector during the December solstice. Especially, the distribution of midlatitude irregularities has hemispheric asymmetry, with a higher occurrence rate in the winter hemisphere. However, the occurrence of midlatitude scintillation is comparable in both hemispheres during the June solstice, and it concentrates in the southern hemisphere during the December solstice. (3) The EPIs concentrate more at the altitudes of Swarm A, while the midlatitude irregularities mainly occur at the altitudes of Swarm B.

Keywords: ionospheric irregularities; phase scintillation; low and middle latitudes; seasonal variations

Citation: Kuai, J.; Wang, K.; Zhong, J.; Wan, X.; Huang, F.; Sun, H.; Chen, J.; Song, X.; Han, H. Analysis of the Ionospheric Irregularities and Phase Scintillation at Low and Middle Latitudes Based on Swarm Observations. *Remote Sens.* **2022**, *14*, 4780. https://doi.org/10.3390/rs14194780

Academic Editors: Chunhua Jiang, Huijun Le, Ercha Aa and Zheng Li

Received: 24 August 2022
Accepted: 21 September 2022
Published: 24 September 2022

1. Introduction

In the past decades, the global navigation satellite system (GNSS) has been widely used around the world, and countless works have been conducted to improve the positioning accuracy and signal reliability of the GNSS. The ionosphere, which has served as a key medium for the GNSS radio signal transmission, would show a great impact on the reliability of the GNSS applications. Specifically, the drastic changes in the ionosphere, which are normally referred to as plasma density irregularities, would directly result in signal attenuation or interruption. Therefore, ionospheric research is an essential aspect of mitigating GNSS error.

The presence of plasma density irregularities in the ionosphere would cause rapid random fluctuations in the amplitude and phase of transionospheric radio waves [1,2]. This phenomenon is called scintillation, which would lead to the reduction of signal quality, and even cause the GNSS satellite's signal tracking failure for receivers. This process is usually called "loss of lock", which may lead to an increase in navigation inaccuracies or even failures [3]. When the fading depth of the signal caused by amplitude scintillation exceeds the fade margin of the receiver, the signal could be covered by background noise; or the shift in frequency caused by phase scintillation exceeds the phase lock loop bandwidth, cycle slips could occur, and the signal could even be lost [4]. The scintillations occur most commonly near the geomagnetic equator at night during solar maximum and at high latitudes [5].

The generation and development of ionospheric density irregularities in different regions correspond to different plasma physical processes and mechanisms. At low latitudes, the most common ionospheric irregularities include equatorial plasma depletion (EPD) and plasma blob. EPD is also referred to as equatorial plasma bubble (EPB) or equatorial spread F (ESF), which characterizes the decrease in plasma density relative to ambient plasma. EPB is the result of Rayleigh–Taylor (R–T) instability at the bottom-side F layer, and it can penetrate through the topside ionosphere [6]. Another low-latitude irregularity is the plasma blob, a high-density structure compared with the surrounding region, but its generation is still unclear [7]. In addition to the above irregularities, there are also sporadic E layers (Es layers) and F region irregularities generated through the Perkins instability at low latitudes [8]. Although the variations of low-latitude irregularities (mainly EPBs) with season, longitude, latitude, local time (LT), and solar activity have been studied, whether the phase scintillation could present similar characteristics and how the low-latitude irregularities modify the phase scintillation are still not clear.

Due to the low occurrence rate of scintillation at middle latitudes, previous studies of ionospheric irregularities have been less concentrated at middle latitudes. However, the medium-scale traveling ionospheric disturbances (MSTIDs) can be observed frequently at nighttime in the midlatitude ionosphere, whose horizontal wavelength is 100–300 km and whose phase velocity is 50–300 m/s. The generation of MSTIDs was originally explained by the Perkins instability. Previous studies have shown that atmospheric gravity waves (AGWs) and sporadic E layer (Es) instability induce the development of the Perkins instability, which in turn drives the formation of nighttime MSTIDs [9–11]. Besides, at middle latitudes, there is a band structure with plasma density enhancement at the nighttime ionosphere, which is often observed around $\pm 40^{\circ}$ geomagnetic latitudes from 23 to 05 LT at the topside ionosphere. The middle-latitudinal band structure at the topside ionosphere may be mainly derived from the ambipolar diffusion of the plasmasphere and the upward plasma drift caused by the equatorward neutral wind along the geomagnetic field line [12]. Whereas research on the general characteristics of the middle-latitudinal band structure has been investigated [3,13], whether the middle-latitudinal band structure includes irregularities and the related characteristics of the irregularities are not clear.

The topside ionospheric irregularities at low latitudes are thought to be the origination of the vertical extension from the bottom ionospheric irregularities. However, recent studies indicate that the topside ionospheric irregularities present particular variations [14–17]. As a polar-orbiting satellite constellation, Swarm had gathered long-term in situ electron density data along the satellite tracks and the topside total electron content (TEC) data for more than 8 years up to now, which provides an opportunity to study the climatological features of global ionospheric irregularities and the corresponding ionospheric scintillation at different local times, latitudes, longitudes, and solar activity levels. In this work, we directly compare the occurrence of irregularities detected by in situ electron density with GNSS signal scintillation based on the platform of Swarm satellites. This study aims to verify whether the occurrence of phase scintillation in the topside ionosphere is caused by in situ irregularities and to further study the differences between the distribution of irregularities and scintillations in the topside ionosphere.

2. Dataset

The Swarm constellation is composed of three satellites (Swarm A, Swarm B, and Swarm C), which were launched on 22 November 2013. During the period from 2014 to 2021, Swarm A and Swarm C flew side by side at an altitude of 500 to 435 km with an orbital inclination angle of 87.35°, whereas Swarm B cruised at 520 to 500 km with an 87.75° inclination angle. It took about 130–140 days for each Swarm satellite to cover all local time.

The in situ electron densities (Ne) measured by the Langmuir probe onboard Swarm constellation are used to investigate the variations of the ionospheric irregularity. In addition, the upward-looking TEC data obtained from Global Positioning System (GPS) observations measured by the Swarm constellation are used to determine the scintillation. The detailed procedure for the upward-looking TEC retrieval was introduced in Yue et al. [18] and Zhong et al. [19]. Note that only nighttime data are used to study the ionospheric irregularities, though the measurement error of Ne could occur at daytime [20].

In this study, we use the Swarm electron density with a sampling rate of 2 Hz and TEC data at a time resolution of 1 s. The study covers a long period from 2014 to 2021. The Swarm data are divided into different seasons (March equinox, June solstice, September equinox, and December solstice) and solar activities. The data within a 90-day window centered on solstice or equinox are selected for each season. The conditions of F107 < 100 and F107 > 100 are defined as low and high solar activities, respectively. Note that due to the data limition, the averaged altitude of the Swarm satellites was higher under high solar activity. In the following, the ionospheric irregularities are detected by RODI, and phase fluctuations of the GPS receiver onboard Swarm are determined by ROTI.

2.1. RODI

Many approaches have been developed to distinguish the irregularities from the in situ electron density, and we take a similar method described by Jin et al. [21]. The ionospheric irregularities are detected with the irregularity parameters derived from the satellite in situ Ne measurements: the rate of change of density (ROD) and the rate of change of density index (RODI).

We calculate the mean electron density with a sliding window of 60 s, and by substracting it from Ne, a high-pass filtered Ne is acquired, which we also call 'detrended Ne'. Then, $\boldsymbol{ROD}$ is obtained as the time derivative of the detrended Ne:

$$\boldsymbol{ROD}(t) = \frac{\boldsymbol{Ne_d}(t + \Delta t) - \boldsymbol{Ne_d}(t)}{\Delta t} \tag{1}$$

where $\boldsymbol{Ne_d}$ represents the detrended $\boldsymbol{Ne}$, and $\Delta \boldsymbol{t}$ is 0.5 s for the Swarm $\boldsymbol{Ne}$ data (with a sampling frequency of 2 Hz). $\boldsymbol{RODI}$ is the standard deviation of $\boldsymbol{ROD}$ at a running window of 20 s, corresponding to the irregularities at a spatial scale of approximately 7.5–150 km.

$$\boldsymbol{RODI}(t) = \sqrt{\frac{1}{N-1} \sum_{t_i = t - \frac{\Delta t}{2}}^{t_i = t + \frac{\Delta t}{2}} \left| \boldsymbol{ROD}(t_i) - \overline{\boldsymbol{ROD}}(t) \right|^2} \tag{2}$$

where $\Delta \boldsymbol{t}$ is the running window size (20 s), $\boldsymbol{N}$ is data number in the running window, and $\overline{\boldsymbol{ROD}}$ is the mean of $\boldsymbol{ROD}$:

$$\overline{\boldsymbol{ROD}}(t) = \frac{1}{N} \sum_{t_i = t - \frac{\Delta t}{2}}^{t_i = t + \frac{\Delta t}{2}} \boldsymbol{ROD}(t_i) \tag{3}$$

2.2. ROTI

To describe the phase fluctuation of GPS signals, Pi et al. [22] defined the rate of TEC index (ROTI) based on the standard deviation of ROT; ROT is the rate of change of TEC. In this study, the slant TEC is converted to the vertical TEC, using only GPS satellites

with elevations greater than 30°, and the altitude of the ionospheric pierce point is set as 850 km. The mean VTEC data in 20 s are calculated as the background to detrend the VTEC, corresponding to a distance of around 150 km traveled by Swarm satellites. The ***ROT*** was calculated and converted to the unit of TECU/min according to the following formula, where $\boldsymbol{i}$ is the corresponding satellite and $\Delta \boldsymbol{t}$ is 1 s:

$$\boldsymbol{ROT}(\boldsymbol{t}) = \frac{\boldsymbol{VTEC}^{\boldsymbol{i}}_{\boldsymbol{t}+\Delta \boldsymbol{t}} - \boldsymbol{VTEC}^{\boldsymbol{i}}_{\boldsymbol{t}}}{\Delta \boldsymbol{t}} \times 60 \quad (4)$$

where ***VTEC*** is the detrended vertical TEC, and ***ROTI*** is obtained by calculating the standard deviation of ***ROT*** in the running windows of 20 s, which corresponds to the phase scintillation at a spatial scale of approximately 7.5–150 km:

$$\boldsymbol{ROTI} = \sqrt{< \boldsymbol{ROT}^2 > - < \boldsymbol{ROT} >^2} \quad (5)$$

where the symbol <> denotes the mean value in the running window.

2.3. An Example of Ionospheric Irregularities

At first, we give an example of ionospheric irregularities near the equator observed by Swarm A during 19:30–19:48 universal time (UT) on 12 October 2021, and the responses of multiple parameters to the irregular structures are shown in Figure 1. Figure 1a displays the electron density (Ne), background density (bNe), and detrended density (detNe) in orange, blue, and yellow, respectively. The double-peak equatorial ionization anomaly (EIA) can be clearly identified during 19:39–19:45 UT. Additionally, there were many ionospheric irregularities, as the electron density oscillated dramatically (mainly from 19:32 to 19:39 and from 19:43 to 19:45 UT) predominantly at the poleward sides of the EIA. By removing the background, it can be seen that the signature of the large-scale EIA structure can be mitigated or ignored, while the small-scale irregularities are reserved.

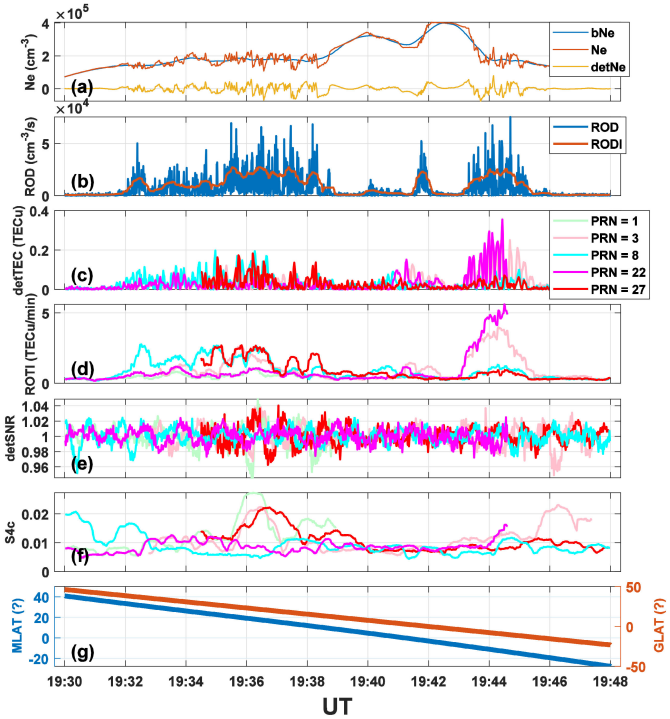

Figure 1. An example of the derived irregularity parameters from Swarm A as a function of UT on 21 December 2021. (**a**) electron density (Ne, red), background electron density (bNe, blue), and the detrended electron density (detNe, orange), (**b**) ROD and RODI, (**c**) detrended TEC, (**d**) ROTI, (**e**) detrended SNR, (**f**) S4c, (**g**) geomagnetic latitude and geographic latitude.

Figure 1b plots the ROD and RODI in blue and orange lines, respectively. To present the amplitude of the electron density fluctuations straightly, only the absolute values of ROD are shown here. The two parameters well reflected the dramatic changes in density observed in Figure 1a. For example, a slight fluctuation in electron density can be observed around 19:42 UT within the EIA region in Figure 1a, which is more obvious in detrended Ne; correspondingly, an apparent fluctuation of ROD and RODI can be seen at the same position in Figure 1b.

Previous studies developed different algorithms for automatic detection of those irregularities [14,23,24]. A key strategy of those algorithms is that, by setting the thresholds of the fluctuation amplitude, the fluctuations can be determined whether they are strong enough to be considered irregularities, rather than noises. Those thresholds can be generally categorized into two types: absolute and relative density perturbations. Previous studies pointed out that the occurrence pattern of the irregularities determined by the absolute density perturbation definition exhibited better agreement with that of the scintillations [25]. Since this work is dedicated to cross-check the in situ plasma irregularities with scintillation events, we then adopt the absolute enhancement/attenuation threshold in the density to detect the ionospheric irregularities. Thus, to avoid the trend of background density like EIA, $RODI > 10^4$ cm^{-3}/s is set as the threshold for determining the ionospheric irregularities. Based on the experiments (not shown) during data processing, if the threshold is set with the fluctuation within ±30%, it has little impact on the statistical results, which indicates the reliability of the threshold selection.

To evaluate the radio signal quality during its transmission through the irregularities, we calculate the phase and amplitude scintillation parameters from the TEC and signal-to-noise ratio (SNR). The vertical TEC is first converted from the STEC calculated by the GPS observation data from the onboard receiver, and the vertical TEC data are detrended by subtracting the mean value in 20 s in each arc, as shown in Figure 1c. In addition, we exclude the data as the GPS satellites flew at elevation angles below 30 degrees. The parameters derived from TEC data show similar oscillations in the corresponding positions, as shown in Figure 1b. Note that these parameters represent TEC fluctuations in the topside ionosphere, and a value of 0.1 is used as the threshold of ROTI to indicate the strong phase scintillation.

The equivalent signal-to-noise ratio (S/N) and S4c index can be derived from the carrier-to-noise ratio (C/N) data released by common geodetic GNSS receivers [26], which provide a new method for the calculation of the amplitude scintillation index. A value of 0.015 is used as the threshold of S4c to indicate the strong amplitude scintillation. To verify the feasibility of this method on a satellite-based receiver, Figure 1e,f displays the detrended S/N and S4c derived from C/N recorded by Swarm A. Similar trends are shown in the detrended SNR and S4c index from GPS satellites from 19:35 to 19:39 UT. However, the significant fluctuations around 19:44 UT were not reflected in the amplitude scintillations.

3. Results and Discussion

3.1. Global Seasonal Distribution

After the detection of the irregularities, the occurrence rate is calculated by the ratio of the irregularity data points to the total data points in a grid with 10° in longitude and 5° in latitude. To systematically present the spatial, seasonal, and solar activity variations of the nighttime ionospheric irregular structures, the occurrence rate of irregularities calculated from RODI at different seasons (March equinox, June solstice, September equinox, and December solstice), altitudes (460 km for Swarm A and 520 km for Swarm B), and solar activities (F107 < 100 and F107 > 100) is compared in geographic coordinates. Figure 2 shows the global distribution of the occurrence rate of irregularities before midnight (18:00–24:00 LT).

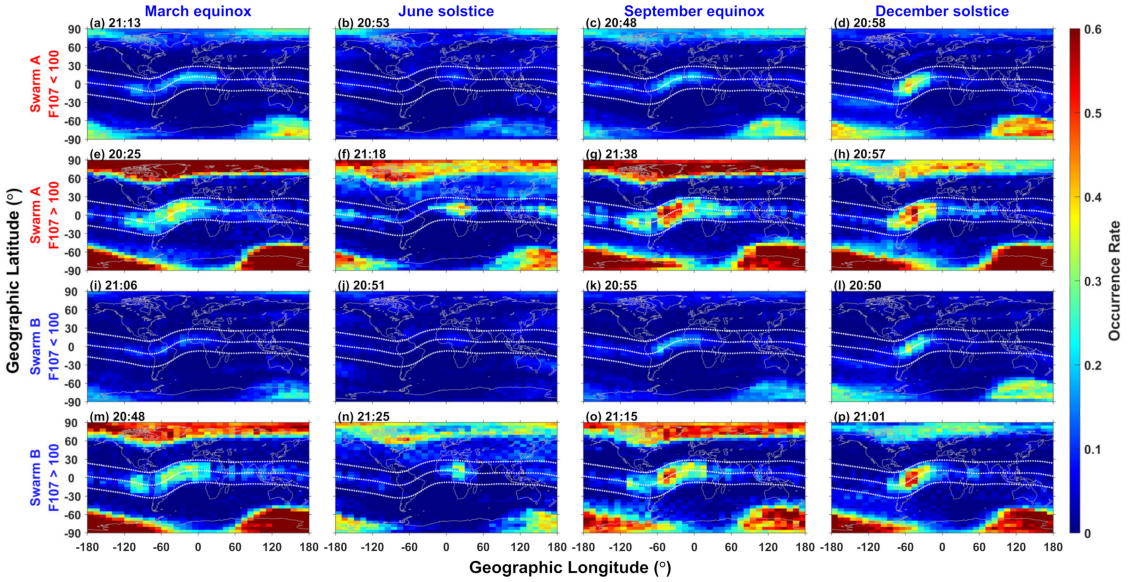

Figure 2. Global distribution of occurrence rate by RODI for different seasons, satellites, and F107 in geographic coordinates before midnight. The mean local time was marked in the subtitle. The pixels has a resolution of 10° in geographic longitude and 2.5° in geographic latitude. The contour lines of the geomagnetic latitudes at ±20° (white line) are also plotted for reference. The color-bar ranges are set as the same at each column. The panels from top to bottom show results for Swarm A (F107 < 100, (**a**–**d**)), Swarm A (F107 > 100, (**e**–**h**)), Swarm B (F107 < 100, (**i**–**l**)), and Swarm B (F107 > 100, (**m**–**p**)), from left to right show results at March equinox, June solstice, September equinox, and December solstice.

During low solar activity for Swarm A observations (Figure 2a–d), the peak occurrence of irregularities was concentrated at low and high latitudes, with the weakest occurrence at middle latitudes. At low latitudes, the occurrence showed a clear seasonal and longitudinal dependence near the geomagnetic equator. Among the four seasons, the occurrence of EPIs (equatorial plasma irregularities) was highest during the December solstice and lowest during the June solstice. The occurrence was similar during March and September equinoxes. The high occurrence rate of EPIs during the March/September equinox showed a longitudinal preference from Africa to South America (Figure 2a,c). During the June solstice, EPIs were concentrated over North Africa, and during the December solstice, they were prevalent at Atlantic to South American longitudes (Figure 2b,d). At middle latitudes, the occurrence rate of irregularities was low in all seasons. Under low solar activity, the symmetrical band structure in the northern and southern hemispheres could be seen at middle latitudes with an occurrence of about 10%, concentrated in the Asia Pacific longitudes, and was more apparent in Swarm B (Figure 2i–l). Under high solar activity, the occurrence rate was larger in the summer hemisphere during the solstices (shown in Figure 2f,h,n,p). At high latitudes, the pattern of occurrence during the equinoxes showed a large value in both hemispheres, especially in the southern hemisphere. The occurrence rate at high latitudes was low during the June solstice, with peak occurrence concentrated in the northern hemisphere (NH), and the occurrence rate only showed great value in the southern hemisphere (SH) during the December solstice.

Under high solar activity (Figure 2e–h), from the observations of Swarm A, the overall occurrence rate of irregularities was higher than that under low solar activity. At low latitudes, the high occurrence rate region of EPIs became significantly larger, compared with that under low solar activity. During the June solstice, in addition to the prominent peak occurrence rate over Africa, an enhanced occurrence can be also observed over the Pacific sector. At middle latitudes, the occurrence of irregularities remained low in all seasons, similar to the results under low solar activity, except for a slight enhancement in

the northern hemisphere during the June solstice (Figure 2f). At high latitudes, the overall occurrence rate was enhanced with increasing solar activity, and the seasonal distribution characteristics remained similar during low solar activity periods.

Many studies have shown that the occurrence of the premidnight EPIs peaks at solar maximum [13,27–29]. In addition, at a given longitude, EPIs occur more frequently when the geomagnetic field lines are aligned with the sunset terminator [13,30]. A small angle between the equatorial geomagnetic line and the sunset terminator could result in a decrease in the flux tube-integrated conductance and, thus, an increase in the growth rate of the R–T instability. For example, in the South American and Atlantic sectors, a small angle would occur from October to March, thus leading to a high occurrence rate in these regions during the December solstice and equinoxes. In addition, transequatorial winds may lead to an increase in local conductivity in the winter hemisphere and a decrease in the summer hemisphere [31,32]. Since the decrease in conductivity would enhance the growth of the R–T instability, it results in a higher occurrence rate in the Asian and African sectors, where the geomagnetic equator is located in the summer hemisphere during the June solstice, and a higher occurrence rate in the American and Atlantic Ocean region during the December solstice.

For Swarm B observations (Figure 2i–p), the overall occurrence of the irregularities decreased, compared with that of Swarm A. At higher altitudes, the region of the high occurrence rate of EPIs became smaller, during all seasons and solar activities. The remaining similar features of solar activity and seasonal distribution are not repeated here. In addition, the occurrence rate of RODI is much low between -60 and 60° longitudes at midlatitudes in the southern hemisphere. The geomagnetic latitude is lower in this region, and the higher occurrence rate at other longitudes should be related to the Weddell Sea Anomaly (WSA) [33].

To compare the in situ observations of irregularities with the topside ionospheric scintillation before midnight, Figure 3 gives the occurrence of phase scintillation based on ROTI results. The occurrence of scintillation showed a good agreement with the characteristics of the irregularities based on RODI. At low and high latitudes, the premidnight irregularities and phase scintillation were positively correlated with solar activity, and they showed similar longitudinal/seasonal patterns. The occurrence rate of phase scintillation at middle latitudes was still at a very low level, which was also a little larger in the summer hemisphere during the solstices under high solar activity (Figure 3f,h,n,p), but the enhanced occurrence rate was almost not visible under low solar activity.

Figure 4 illustrates the occurrence rate of irregularities after midnight, with a smaller color-bar range of 0–0.3, which is different from that of Figure 2. At low latitudes under low solar activity, the occurrence rate of irregularities was higher during the solstices than during the equinoxes (Figure 4a–d,i–l). Under high solar activity, the overall occurrence rate of EPIs was higher than that under low solar activity. The peak occurrence rate of EPIs during the equinoxes was concentrated in the region from the east coast of South America to Africa (Figure 4e–h), with an eastward movement compared with the distribution before midnight (Figure 2e–h). At middle latitudes under low solar activity, a striped structure of enhanced occurrence can be clearly observed at Asia Pacific longitudes in both hemispheres. The enhanced occurrence at the middle latitudes was most pronounced during the June solstice and least pronounced during the equinoxes. The irregularities at middle latitudes occurred more frequently in the winter hemisphere (Figure 4b,d,j,l). In addition, the enhanced midlatitude occurrence during the December solstice covered a wider longitude range from Asia Pacific to the America Atlantic. Additionally, the occurrence rate at middle latitudes decreased as solar activity increased. Under low solar activity, for Swarm B observations, the overall occurrence rate was decreased at low and high latitudes but enhanced slightly at middle latitudes compared with Swarm A, which indicates that the midlatitude irregularities might be more concentrated at the altitude of Swarm B.

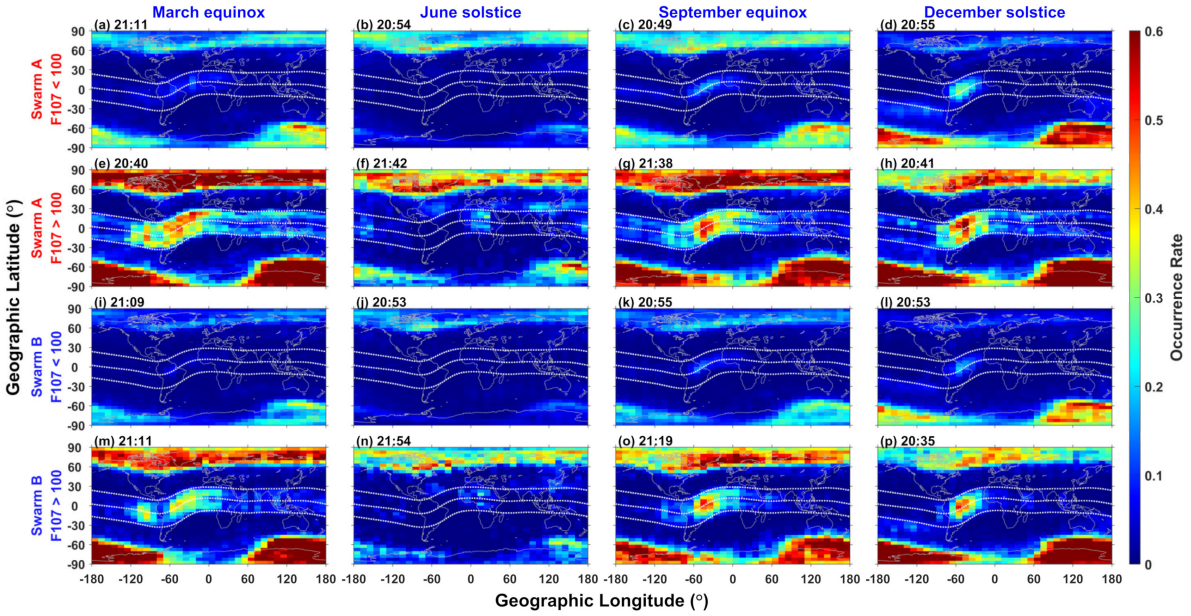

Figure 3. Same as Figure 2 but for ROTI. The panels from top to bottom show results for Swarm A (F107 < 100, (**a**–**d**)), Swarm A (F107 > 100, (**e**–**h**)), Swarm B (F107 < 100, (**i**–**l**)), and Swarm B (F107 > 100, (**m**–**p**)), from left to right show results at March equinox, June solstice, September equinox, and December solstice.

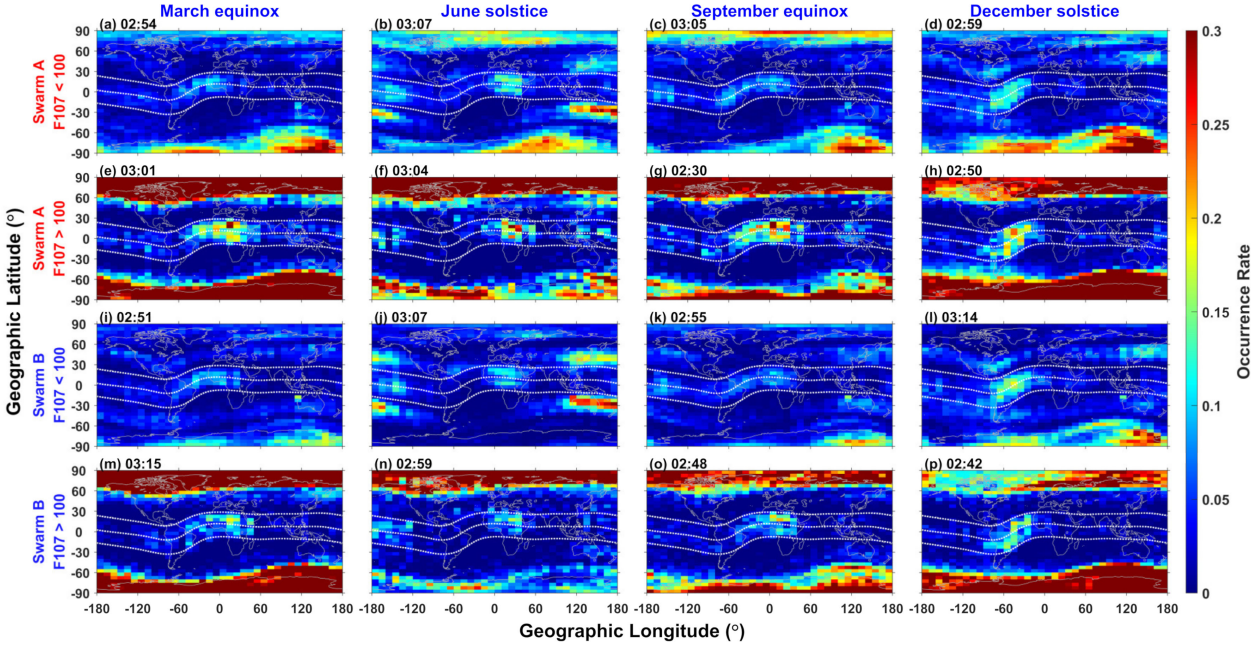

Figure 4. Same as Figure 2 but after midnight. The panels from top to bottom show results for Swarm A (F107 < 100, (**a**–**d**)), Swarm A (F107 > 100, (**e**–**h**)), Swarm B (F107 < 100, (**i**–**l**)), and Swarm B (F107 > 100, (**m**–**p**)), from left to right show results at March equinox, June solstice, September equinox, and December solstice.

Figure 5 shows the postmidnight occurrence rate of phase scintillation. Due to the weaker topside ionospheric scintillation, the range of the color bar is set to 0–0.1. The occurrence of scintillation at low and high latitudes exhibited similar seasonal and solar activity variations to that of the postmidnight irregularities. At middle latitudes, an enhanced occurrence rate of phase scintillation was also seen during the June solstice

by both satellites (Figure 5b,j); however, Swarm A at lower altitudes registered a higher occurrence rate than Swarm B at higher altitudes. Note that this altitudinal dependence of the occurrence of scintillation contradicts the occurrence rate of midlatitude irregularities, as the latter argument showed greater value at the altitudes of Swarm B (Figure 4b,j).

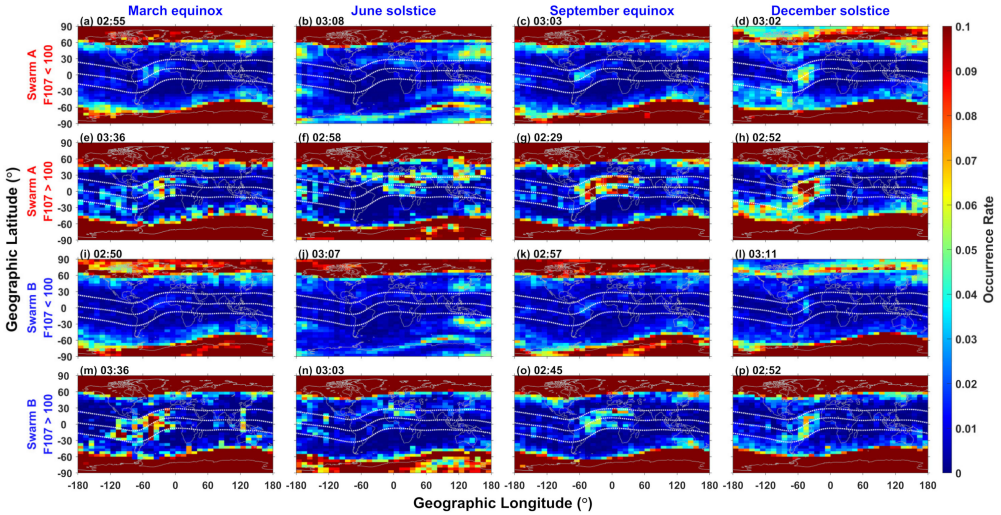

Figure 5. Same as Figure 2 but for ROTI after midnight. The panels from top to bottom show results for Swarm A (F107 < 100, (**a**–**d**)), Swarm A (F107 > 100, (**e**–**h**)), Swarm B (F107 < 100, (**i**–**l**)), and Swarm B (F107 > 100, (**m**–**p**)), from left to right show results at March equinox, June solstice, September equinox, and December solstice.

At low latitudes, the occurrence rate of EPIs after midnight was positively correlated with solar activity, using absolute density perturbations. This result is in contrast to that of Aa et al. [27], who detected EPIs by high pass filters and showed a negative correlation between postmidnight EPIs and F107 after midnight. In a study by Huang et al. [25], the overall occurrence rate of identifying EPIs based on relative density perturbations was negatively correlated with solar activity, as can be seen in their Figures 3 and 4. Wan et al. [29] identified EPIs by a combination of absolute and relative criteria, and in their Figure 5, it can be seen that the occurrence of postmidnight EPIs was higher overall under high solar activity than under low solar activity. Both absolute and relative density perturbations can be used as a criterion for identifying ionospheric irregularities. The lower ambient electron density after midnight may lead to a lower fluctuation in the electron density of EPIs as well, thus making the occurrence of identification based on absolute criteria positively correlated with solar activity. Additionally, for the opposite feature identified based on relative criteria after midnight, it was found that gravity wave activity is stronger at low solar flux levels [34], which may lead to an increase in the occurrence of EPIs under low solar activity.

At middle latitudes, some studies have shown that the neutral-particle density of the upper atmosphere is highest at the equinoxes and lower during the solstices [35]. Meanwhile, the growth rate of the Perkins instability is inversely proportional to neutral-particle density, and the amplitude of gravity waves becomes greater at low neutral-particle density [10]. These facts may lead to the high occurrence of irregularities at middle latitudes during the solstices.

Besides, due to the lower altitudes of Swarm A, the corresponding integration path of TEC is longer and may contain more irregularities, so both low and middle latitudes have a greater occurrence rate of scintillation on Swarm A.

For further comparison with the amplitude scintillation in the top ionosphere, Figure 6 shows the S4c index calculated from the carrier-to-noise ratio. The occurrence rate of amplitude scintillation was obviously different from the RODI and ROTI. The occurrence rate of amplitude scintillation (S4c) was higher at low and high latitudes, was lowest

at middle latitudes, and increased with the increasing solar activity. The S4c index also displayed a clear longitudinal variation of a higher occurrence rate over the low latitude region of the Asian sector under low solar activity. The amplitude scintillation of the top ionosphere calculated from C/N was very weak (an amplitude scintillation index greater than 0.3 in the output of a general ground-based scintillation receiver is considered to be a strong scintillation), and showed no seasonal dependence.

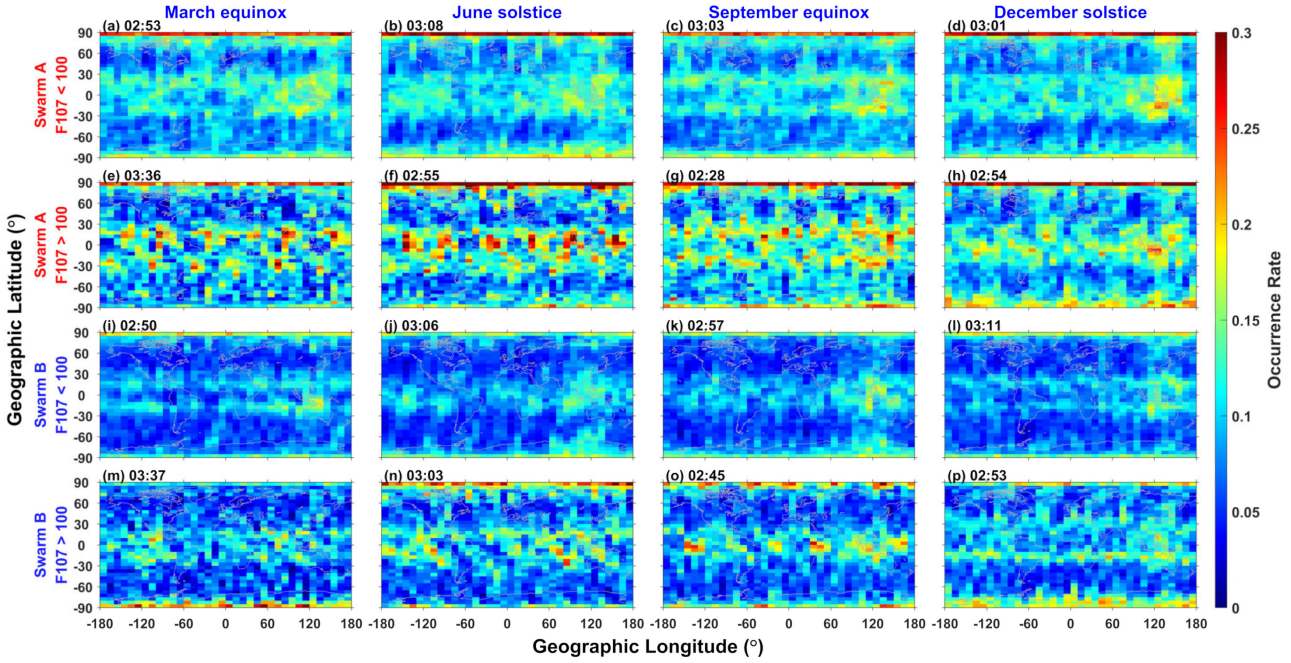

Figure 6. Same as Figure 2 but for S4c after midnight. S4c denotes the approximate S4 index calculated from the carrier-to-noise ratio. The panels from top to bottom show results for Swarm A (F107 < 100, (**a**–**d**)), Swarm A (F107 > 100, (**e**–**h**)), Swarm B (F107 < 100, (**i**–**l**)), and Swarm B (F107 > 100, (**m**–**p**)), from left to right show results at March equinox, June solstice, September equinox, and December solstice.

3.2. Characteristics at Low Latitudes

Figure 7 exhibits the LT variations of the occurrence rate of plasma irregularities identified by RODI near the geomagnetic equator (±10°). For the Swarm A results (Figure 7a–c), the occurrence rate was higher during the December solstice and the two equinoxes and lowest during the June solstice. This could be related to the low-level background Ne during the June solstice, which leads to a small perturbation magnitude of EPIs; thus, the occurrence rate is lower based on the extract method with the absolute enhancement/attenuation threshold. The LT variations during the December solstice and the equinoxes showed similar characteristics. During the December solstice, the occurrence rate began to increase rapidly at about 19:00 LT, peaked at around 22:00 LT, and remained at high values before midnight; then it continued to decrease after midnight (Figure 7c). The prereversal enhancement (PRE) after sunset [36], corresponding to equatorial upward E×B drift velocity, is conducive to the development of the R–T instability and the EPI formation. Therefore, the occurrence rate of EPIs usually peaks before midnight.

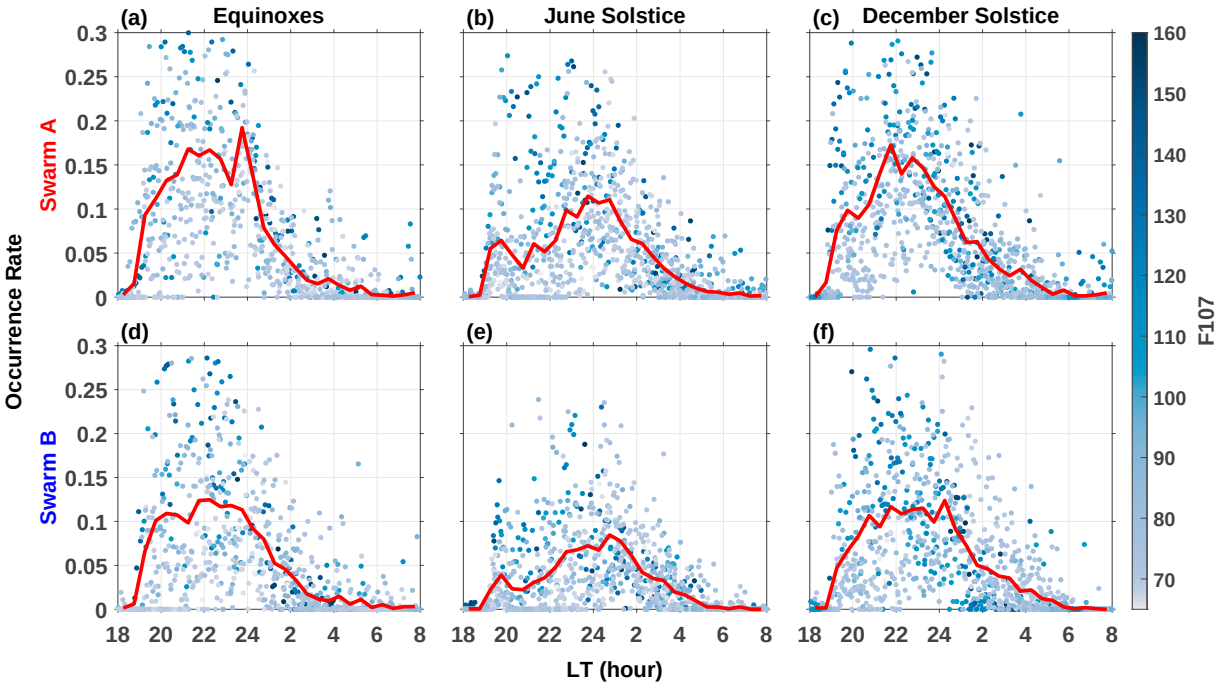

Figure 7. Variations of the plasma irregularity occurrence rate as a function of LT by RODI for different F107 and satellites near the geomagnetic equator (±10°). The panels from left to right show results during the equinoxes (**a**,**d**), June solstice (**b**,**e**), and December solstice (**c**,**f**), from top to bottom show results for Swarm A and Swarm B. The red lines display the 0.5 h averaged variation of the occurrence. Each dot indicates the average daily occurrence and local time of the satellite's ascending and descending orbits.

However, the situation was slightly different during the June solstice (Figure 7b,e), the whole occurrence rate was lower compared with other seasons, but the increase in occurrence rate stayed until midnight and peaked at around 1 LT (Figure 7b,e). Wan et al. [29] showed that the occurrence of EPIs after midnight at an African longitude was comparable to or even higher than that before midnight during the equinoxes and June solstice. For the mechanism of EPI formation after midnight, some studies have suggested that the postmidnight EPIs are not a continuation of the premidnight EPIs during the June solstice, but they are newly generated due to an increase in the growth rate of the R–T instability caused by an upward drift of the plasma [37]. The duration of the vertical drift of the plasma at African longitudes is longer during the June solstice compared with other seasons. In addition, due to the equatorward meridional neutral winds associated with midnight temperature maximum (MTMs), the F-layer height rises significantly after midnight during the June solstice, leading to an increase in the growth rate of the R–T instability. Additionally, Huang and Kelley [38] used numerical simulations to investigate the properties of large-scale equatorial F-region irregularities generated by gravity waves and showed that a zonally propagating gravity wave can seed the R–T instability, and the spatial resonance of gravity wave and plasma motion can promote the formation of a plasma bubble. Otsuka [39] suggested that circularly phased gravity waves can generate electric field perturbations through the F-region dynamo mechanism, thereby initiating the R–T instability effectively. Furthermore, Miller et al. [40] suggested that MSTID accompanied by a polarized electric field can also seed the R–T instability at low latitudes after midnight. Overall, after midnight, gravity waves, MSTID, and equatorial meridional winds might all contribute to EPIs. If interpreted as the postmidnight EPIs are mostly the continuation of EPIs that were generated before midnight, then it cannot explain that the peak of the June solstice occurred after midnight. Thus, the peak occurrence rate after

midnight during the June solstice may be a combination of EPIs already generated before midnight and the newborn EPIs after midnight.

Previous studies have shown that the EPIs with great perturbation magnitudes of plasma density could cause amplitude scintillation obviously [25]. However, how the EPIs affect phase scintillation is still not clear. In comparison with the occurrence of the irregularities, Figure 8 shows the same occurrence rate distribution calculated from ROTI, representing the topside ionospheric phase scintillation. There is a clear difference in the occurrence of the ROTI and RODI. As expected, the ROTI occurrence rate was much smaller than RODI. The enhancement of the scintillation occurrence rate before midnight during the December solstice and the equinoxes was more consistent with the results of EPIs as shown in Figure 7. During the equinoxes, the occurrence rate increased sharply from 18:00 to 20:00 LT, and after 20:00 LT, the occurrence rate began to fall steadily until 2:00 LT, remaining at an extremely low level throughout the postmidnight period. However, during the June solstice, the occurrence rate of ROTI was slightly higher before midnight than after midnight and presented a very low level at all LT. We can see that the total phase scintillation at the topside ionosphere is not always sensitive to the EPIs after midnight. Note that, unlike the in situ observed irregularities, the scintillation in this study is indicative of the signal being between the Swarm satellites and the GPS satellites. Otsuka et al. [41] conducted continuous observations of the field-aligned irregularities (FAI) over Indonesia at night and found that the FAI was not accompanied by GPS scintillation after midnight. The background electron density in the top ionosphere is low after midnight, and there is little fluctuation in the total electron density of topside ionospheric irregularities, which may not generate significant scintillation. Note that small-scale plasma perturbations may not be identified by RODI, but they could cause phase scintillations. During the postmidnight hours, the small-scale plasma perturbations that cause phase scintillations could dissipate more quickly. As a consequence, the phase scintillations could be at a low level after midnight.

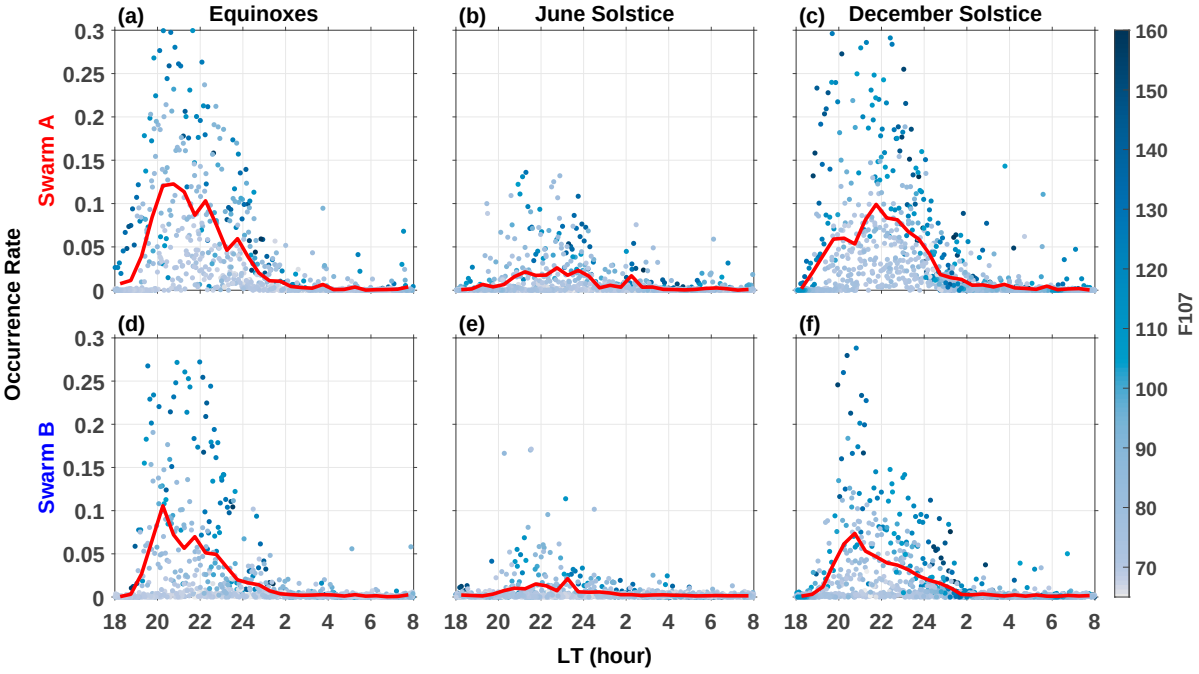

Figure 8. Same as Figure 7 but for ROTI. The panels from left to right show results during the equinoxes (**a**,**d**), June solstice (**b**,**e**), and December solstice (**c**,**f**), from top to bottom show results for Swarm A and Swarm B.

In addition to the solar activity and LT variations, Figure 9 shows the season-longitude variations of the irregularities and scintillation occurrence within ±10° geomagnetic lat-

itudes during the whole night. During the period of low solar activity (Figure 9a,b), the occurrence pattern displayed larger values from the September equinox to the March equinox (Doy 270-80; Doy means the day of the year), appearing in the Atlantic American sector. The region with a high occurrence rate stretched eastward from 60°W to 20°E longitude during Doy 1–90. Later, around Doy 100, the region of high occurrence rate began to gradually separate into two parts, toward the east and the west. Then, during Doy 120–250, two regions of high occurrence rate were observed over the African and Pacific regions, but the overall occurrence decreased. Around the September equinox, the two separated regions with high occurrence rate began to merge into one again. Finally, the main peak occurred around 20°–70°W longitudes during the December solstice. The overall occurrence rate increased under high solar activity (Figure 9c,d, with a larger color-bar range). In addition, it is interesting to note that the main peak after the September equinox occurred around Doy 290, about 2 months earlier, compared with the periods under low solar activity (Doy 350).

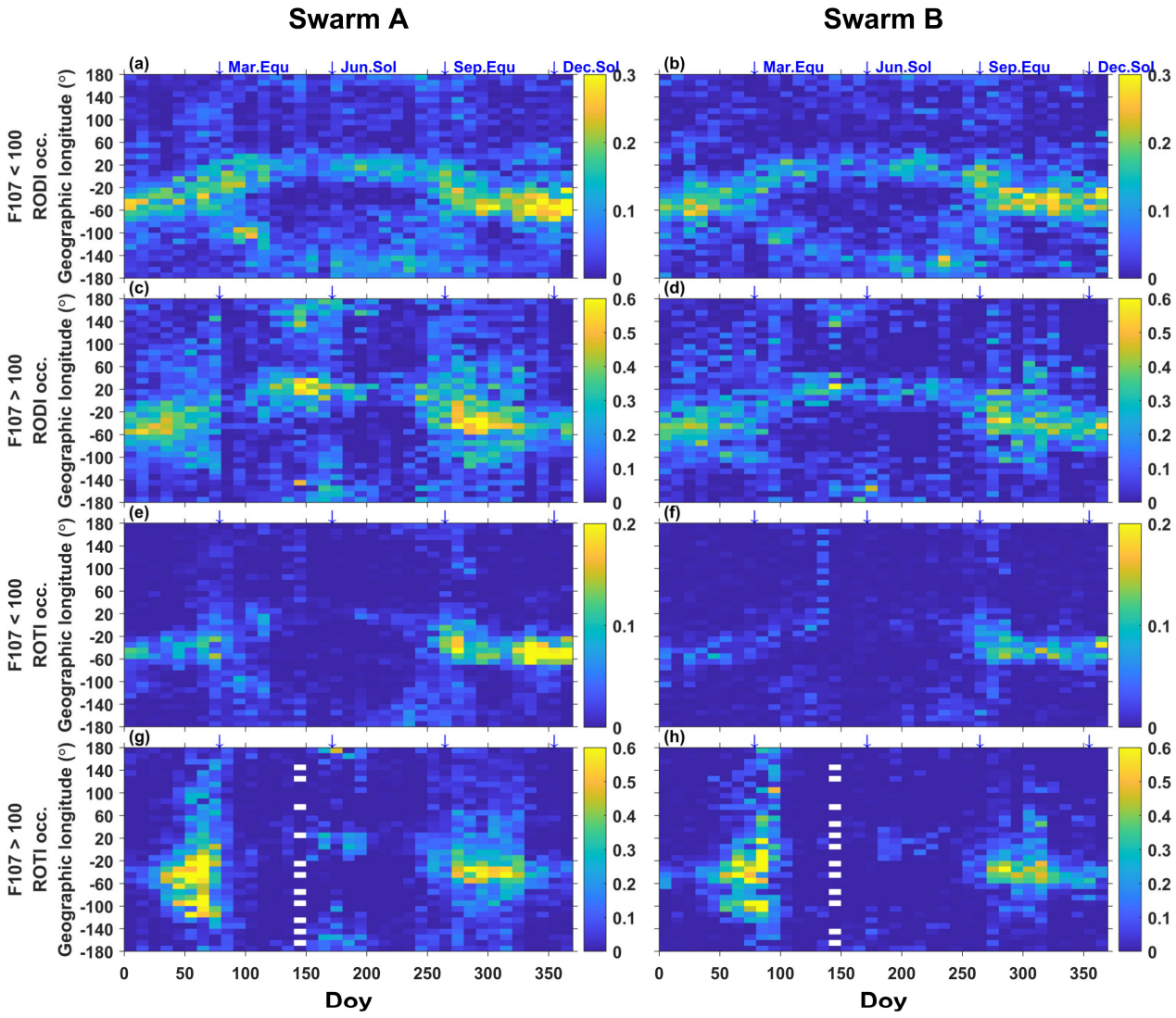

Figure 9. Variations of the plasma irregularity occurrence rate as a function of Doy and longitudes. The equinoxes and solstices are indicated by the arrows on the top of each panel. The panels from top to bottom show results for RODI occurrence (F107 < 100, (**a**–**b**)), RODI occurrence (F107 > 100, (**c**–**d**)), ROTI occurrence (F107 < 100, (**e**–**f**)), and ROTI occurrence (F107 > 100, (**g**–**h**)), from left to right show results for Swarm A and Swarm B.

The same distributions of topside ionospheric phase scintillation are shown in Figure 9e–h. The overall occurrence rate in Swarm A was significantly higher. Under low solar activity, the scintillation distribution was quite similar to the result of RODI, though with a lower occurrence rate, especially around the June solstice. Under high solar activity, the main peak near the September equinox appeared earlier than that during periods of low solar activity, similar to the results of RODI. Additionally, the RODI and ROTI distributions showed some discrepancy, as the longitudinal distribution of the peak occurrence rate of ROTI before the March equinox was wider. The greater ROTI occurrence might be related to the small-scale plasma perturbations, and this needs further confirmation. During the June solstice, the phase scintillation did not show a corresponding occurrence compared with the results of RODI, and it may be caused by ROTI's insensitivity to new irregularities generated after midnight.

3.3. Characteristics at Middle Latitudes

We note that the occurrence rate of irregularities at middle latitudes was much lower than that at low or high latitudes (Figures 2 and 4). To further study the variations of irregularities at middle latitudes, Figure 10 displays the local time variations of midlatitude irregularities' (±30°–±40°) occurrence rate identified by RODI. During the equinoxes, the occurrence rate was lowest, and the occurrence rate after midnight was higher than that before midnight. During the June solstice, the occurrence rate of midlatitude irregularities reached the highest level, compared with the other seasons. In Figure 10b,e, the irregularities started to appear at about 20:00 LT, and the first peak occurrence was witnessed at 21:00 LT. Afterward, the occurrence kept growing and reached its maximum at about 03:00 LT. Then the occurrence rate of the irregularities decreased rapidly during 03:00–06:00 LT. During the December solstice, the LT variations were similar to those during the June solstice, but at a smaller magnitude.

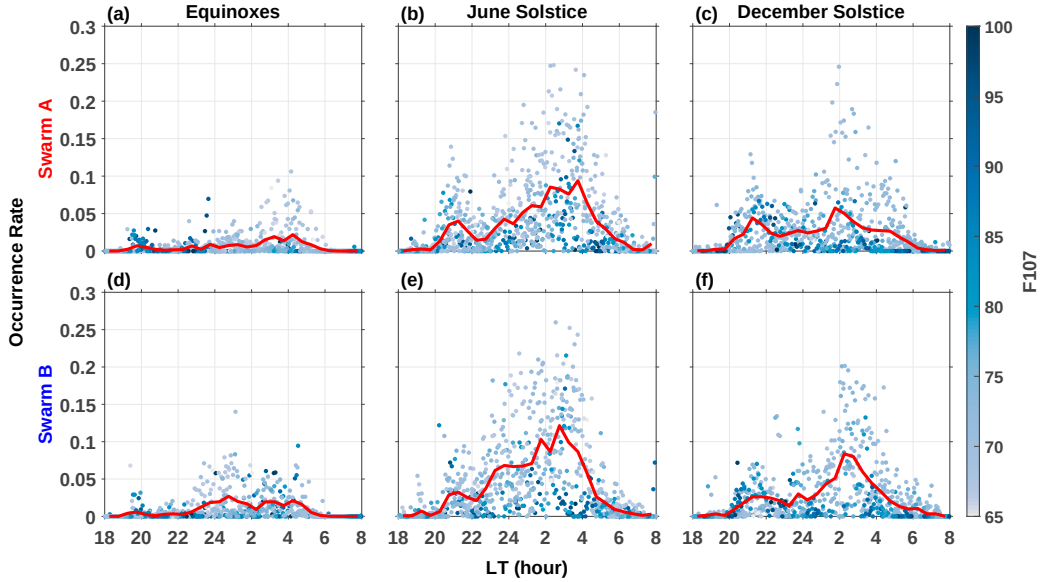

Figure 10. Variations of the plasma irregularity occurrence rate as a function of LT by RODI for different F107 and satellites at midlatitude (±30°–±40° geomagnetic latitudes). The panels from left to right show results during the equinoxes (**a**,**d**), June solstice (**b**,**e**), and December solstice (**c**,**f**), from top to bottom show results for Swarm A and Swarm B. The red lines display the 0.5 h averaged variation of the occurrence. Each dot indicates the average daily occurrence and local time of the satellite's ascending and descending orbits.

To further investigate solar activity dependence, Figure 11 shows the postmidnight occurrence rate calculated by the RODI of midlatitude irregularities with F107. Note that the range of the occurrence rate is 0–0.15 for the equinoxes and 0–0.3 for the solstices. It can be seen that the solar activity dependence of the occurrence rate exhibits negative trends

after midnight, and the midlatitude irregularities only have a larger occurrence rate around the solar minimum. Zhong et al. [12] found that the middle-latitudinal band structure became more pronounced as solar activity decreased. The irregularities at middle latitudes exhibited similar solar activity dependence features to the middle-latitudinal band structure. A large number of observations suggested that the occurrence of MSTID at night is inversely correlated with solar activity [14,42], which is consistent with the characteristics of observed midlatitude irregularities in this study. Although many mid-latitude irregularities have been explained by the Perkins instability, the problem with the Perkins instability theory is that the growth rate is too low to produce significant irregularities in the F region. Some studies have shown that the occurrence rate of sporadic E layer (Es) instability is higher under low solar activity at nighttime [43], and an electrodynamically coupled E and F region containing Es instability would lead to a faster growth rate of the Perkins instability at middle latitudes [44]. Thus, it can be explained that mid-latitude irregularities are higher under low solar activity.

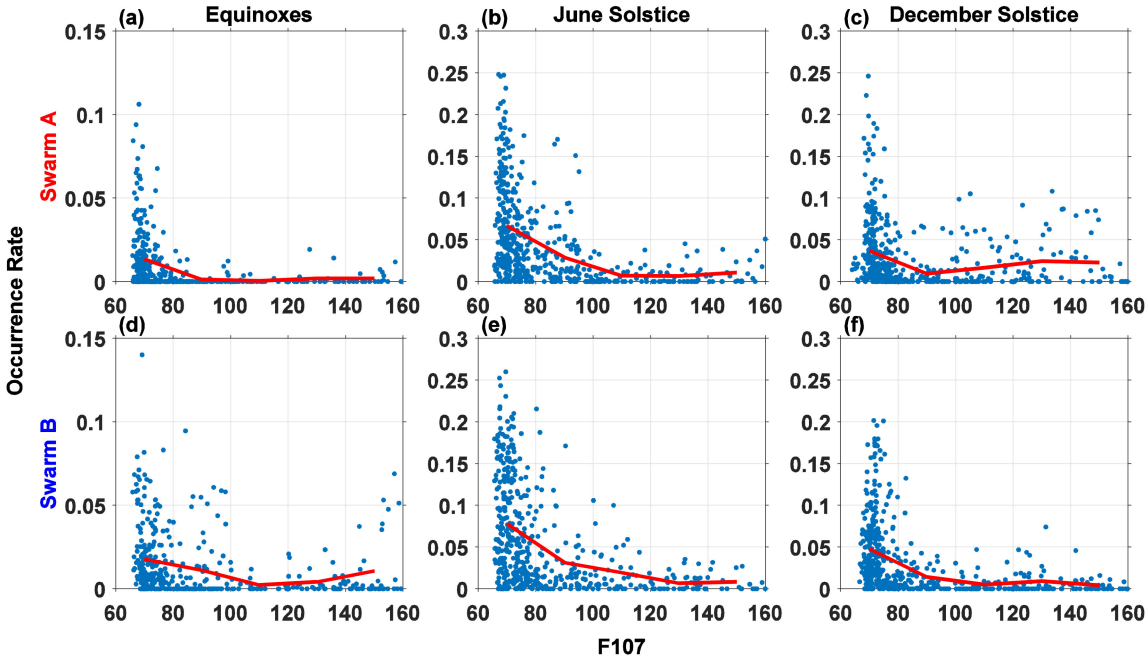

Figure 11. Variations of the plasma irregularity occurrence rate as a function of F107 after midnight by RODI for different satellites at middle latitudes (±30°–±40° geomagnetic latitudes). The panels from left to right show results during the equinoxes (**a**,**d**), June solstice (**b**,**e**), and December solstice (**c**,**f**), from top to bottom show results for Swarm A and Swarm B. The red lines are connected by the mean values of the F107 index every 20 sfu.

Figure 12 displays the season-longitude variations of the midlatitude irregularities and scintillation occurrence rate after midnight. During the equinoxes, the occurrence was the lowest in both hemispheres; this feature also can be seen in Figures 10 and 11. The midlatitude irregularities had a longitudinal preference over the Pacific, from Doy 120 to 230. During Doy 320-40, the large values concentrated over the west of America and the Pacific. In addition, we can see the obvious hemispheric asymmetry. During the June solstice, midlatitude irregularities were evident in the winter hemisphere. During the December solstice, the occurrence was slightly stronger in NH than in SH and peaked around 60°–100°W (Figure 12b), which is in good agreement with previous results in Figures 4 and 5. Some studies have shown that the middle-latitudinal band structure appeared more frequently in the winter hemisphere during the June solstice and under low solar activity [12]. The middle-latitudinal band structure may promote the creation of irregularities. In addition, Park et al. [45] found that midlatitude plasma density fluc-

tuations also showed a strong hemisphere asymmetry, with a preference for the summer hemisphere based on Challenging Mini-Satellite Payload (CHAMP) (altitude ~400 km) and Korea Multi-Purpose Satellite-1 (KOMPSAT-1) (~685 km) observations. Wan et al. [42] showed that the northern and southern hemisphere occurrence of MSTID after midnight even reverses as solar activity decreases. Unlike the MSTID signature, the midlatitude irregularities from Swarm (~450–500 km) occurred more frequently in the winter hemisphere after midnight under low solar activity, based on results from Figures 10–12. Su et al. [14] used Republic of China Satellite 1 (ROCSAT-1) to extract midlatitude irregularities and found that their predominant occurrence was in the winter hemisphere and after midnight. Further research is needed on the hemispheric asymmetry of midlatitude irregularities.

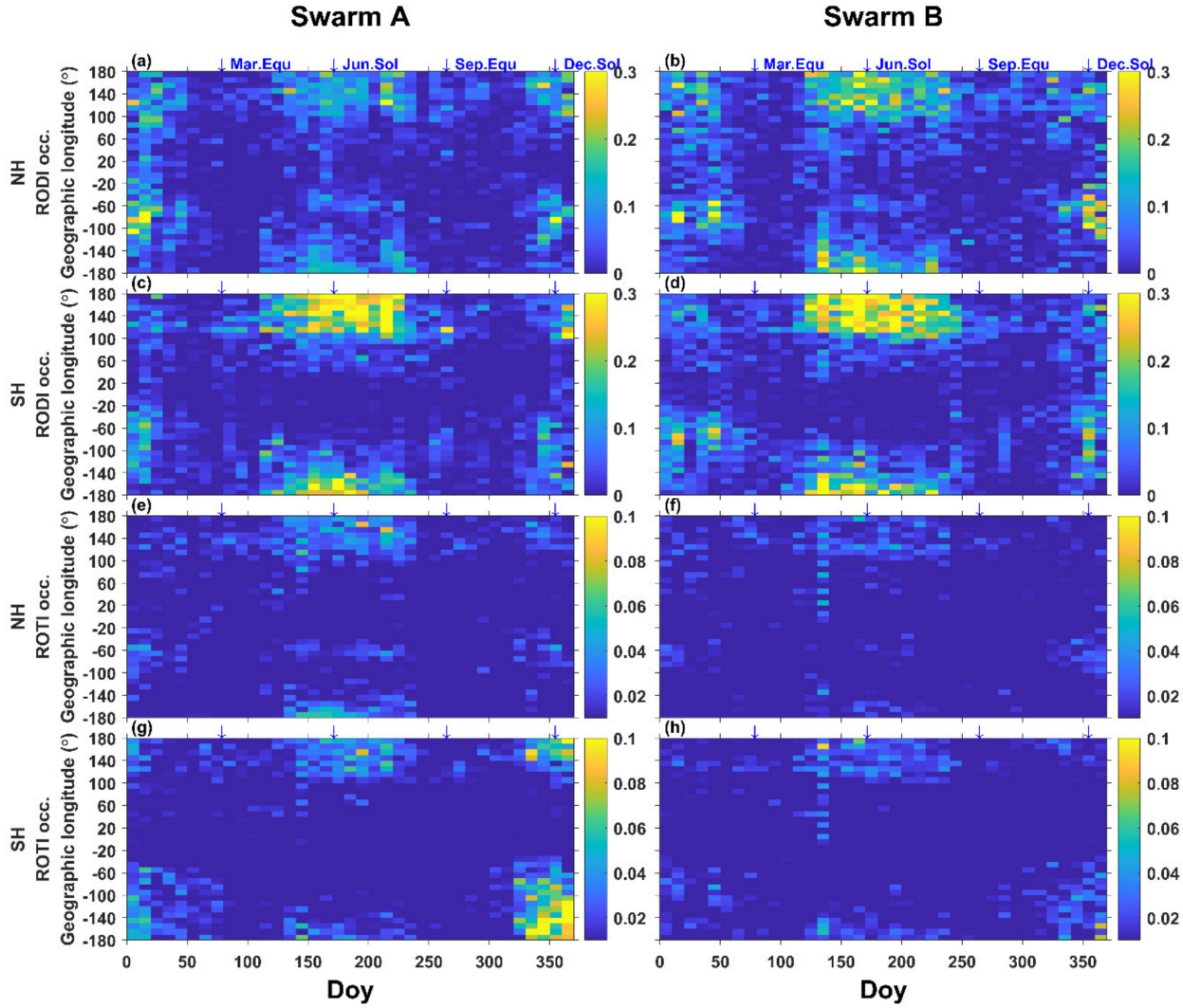

Figure 12. Variations of the plasma irregularity occurrence rate by RODI and ROTI as a function of Doy for different satellites at middle latitudes during Doy 0–360, F107 < 100. The panels from top to bottom show results for RODI occurrence in northern hemisphere (**a**,**b**), RODI occurrence in southern hemisphere (**c**,**d**), ROTI occurrence in northern hemisphere (**e**,**f**), and ROTI occurrence in southern hemisphere (**g**,**h**), from left to right show results for Swarm A and Swarm B. Note that in order to distinguish peak values in different periods, color-bar ranges for irregularities and scintillation occurrence are set differently.

In order to study the influence of middle-latitude irregularities, we inspected the same distribution of topside ionospheric phase fluctuations, as shown in Figure 12e–h. The overall occurrence rate in Swarm A was significantly higher than in Swarm B, especially

in SH. Although the occurrence rate identified by ROTI was lower than that of RODI, their season-longitude variations were consistent, and similar features are not discussed here. However, unlike the former, the middle-latitude topside ionosphere did not produce strong hemispheric asymmetry in scintillation. During the June solstice, the scintillation difference in both hemispheres was not significant. However, during the December solstice, the occurrence was stronger in SH than in NH, mainly concentrated in the southwest Pacific to South America. Small-scale plasma perturbations may not be identified by RODI, but they could cause phase scintillations. The differences between the scintillation and the irregularities' distribution characteristics should be associated with the scale size of irregularities. However, at midlatitudes, the differences also suggest that scintillation in the topside ionosphere could be also influenced by other factors.

Topside ionospheric scintillation may be also related to the distribution of Ne at higher altitudes. In a study by Zhong et al. [12], the Ne distribution at an altitude of 800 km can be seen in their Figures 4 and 5. During the June solstice, the Ne over the Pacific longitudes at middle latitudes in both hemispheres is comparable and symmetrical at 800 km, which is similar to the scintillation results (Figure 12g,h). During December solstice, the electrons are significantly higher at middle latitudes in the southern hemisphere and are concentrated at Weddell Sea Anomaly (WSA) longitudes (from South America to the central Pacific region), which is more consistent with the distribution of high scintillation occurrence during the December solstice in the southern hemisphere (Figure 12g,h). The WSA behavior may be due to ionospheric long-term photoionization during the local summer period and vertical plasma drift caused by neutral winds under geomagnetic field geometry effects [33]. Meanwhile, the higher scintillation occurrence in Swarm A may be explained by the ionospheric irregularities mainly occurring at lower altitudes. The higher absolute perturbations in the electron density of irregularities is more likely to cause scintillation. More observations are needed to verify these inferences.

4. Conclusions

In this work, the electron density and TEC data in 8 years' measurements from the Swarm constellations are utilized to study the occurrence rate of global ionospheric irregular structures and the phase scintillation in the topside ionosphere. The occurrence patterns are analyzed by season, local time, longitude, latitude, and solar activity. The scintillation mainly presents consistent results with the irregularities at low latitudes, but the scintillation shows many differences from the irregularities at middle latitudes. The main results are summarized as follows:

1 At low latitudes, the occurrence rate of postmidnight EPIs is generally decreased, except during the June solstice. During the June solstice, a large number of EPIs appear after midnight, resulting in the occurrence rate peaks at around 01:00 LT. The occurrence rate of EPIs displays an increasing trend with the increasing solar activities. The topside ionospheric scintillation shows relatively consistent results with EPIs, while the scintillation occurrence is quite weak during the June solstice. These results indicate that EPIs contribute most of the topside ionospheric scintillation, but the scintillation could also depend on other factors.

2 The midlatitude irregularities mainly occur after midnight, and the occurrence rate is negatively correlated with solar activity and lowest during the equinoxes and highest during the June solstice. The occurrence rate presents hemispheric asymmetry and is higher in the winter hemisphere than in the summer hemisphere during the solstices. During the June solstice, the peak occurrence rate is concentrated in the Pacific sector, whereas during the December solstice, the peak is seen in the American sector. However, the topside ionospheric scintillation shows many differences from the irregularities. The topside ionospheric scintillation has no significant hemispheric asymmetry during the June solstice and is concentrated in the southern hemisphere during the December solstice, which might be related to the background electron density in the topside ionosphere after midnight.

3 The EPIs concentrate more at the altitudes of Swarm A, while the midlatitude irregularities mainly occur at the altitudes of Swarm B. At both low and middle latitudes, topside ionospheric scintillation has a higher occurrence in Swarm A observations, which might be related to the longer integration path of TEC, resulting in more irregularities for the signal to cross.
4 In addition, there are latitudinal and longitudinal dependences in the global distribution of S4c-based irregularities. However, due to the absence of seasonal dependence, the equivalent scintillation index S4c on the satellite needs further study.

Author Contributions: Conceptualization, J.K., K.W., J.Z. and X.W.; methodology, J.Z. and X.W.; software, K.W., H.S., J.C., X.S. and H.H.; validation, J.K., J.Z., X.W. and F.H.; formal analysis, K.W., X.S. and H.H.; investigation, K.W., X.W. and H.S.; resources, J.K., K.W., J.Z., X.W. and X.S.; data curation, K.W., J.C., X.S. and H.H.; writing—original draft preparation, K.W. and J.Z.; writing—review and editing, J.K., K.W., J.Z., X.W. and F.H.; visualization, J.K., K.W., J.Z. and X.W.; supervision, J.K. and J.Z.; project administration, J.K. and J.Z.; funding acquisition, J.K. and J.Z. All authors have read and agreed to the published version of the manuscript.

Funding: This research was funded by the National Natural Science Foundation of China, grant numbers: 41831070, 41804153, 41804150, and 42104169; the Strategic Priority Research Program of the Chinese Academy of Sciences, grant number: XDB41000000; Guangdong Basic and Applied Basic Research Foundation, grant numbers: 2021A1515011216 and 2022A1515011580; the Natural Science Foundation of Jiangsu Province, grant number: BK20180445; the seventh Young Elite Scientists Sponsorship Program by China Association for Science and Technology, grant number: 2021QNRC001; Shanghai Aerospace Science and Technology Innovation Fund, grant number: SAST2021-075; Key Laboratory Stability Support Fund, grant number: HTKJ2022KL504017; the China Postdoctoral Science Foundation, grant number: 2020M6830265; the Fundamental Research Funds for the Central Universities, Nanjing University of Aeronautics and Astronautics, grant number: NP2022449, and Sun Yat-sen University, grant number: 2021qntd29; the Joint Open Fund of Mengcheng National Geophysical Observatory, grant number: MENGO-202018; the Opening Funding of the Chinese Academy of Sciences dedicated for the Chinese Meridian Project; and the Open Research Project of Large Research Infrastructures of CAS—"Study on the interaction between low/mid-latitude atmosphere and ionosphere based on the Chinese Meridian Project".

Data Availability Statement: The European Space Agency provides the Swarm data on https://swarm-diss.eo.esa.int/, accessed on 1 August 2022. The F107 index can be accessed at https://omniweb.gsfc.nasa.gov/, accessed on 1 August 2022.

Acknowledgments: We thank the European Space Agency for providing the Swarm data and NASA/Goddard Space Flight Center for providing the F107 index.

Conflicts of Interest: The authors declare no conflicts of interest.

References

1. Wernik, A.W.; Secan, J.A.; Fremouw, E.J. Ionospheric irregularities and scintillation. *Adv. Space Res.* **2003**, *31*, 971–981. [CrossRef]
2. Hey, J.S.; Parsons, S.J.; Phillips, J.W. Fluctuations in cosmic radiation at radio-frequencies. *Nature* **1946**, *158*, 234. [CrossRef] [PubMed]
3. Xiong, C.; Stolle, C.; Lühr, H. TheSwarmsatellite loss of GPS signal and its relation to ionospheric plasma irregularities. *Space Weather* **2016**, *14*, 563–577. [CrossRef]
4. Sreeja, V.; Aquino, M.; Elmas, Z.G.; Forte, B. Correlation analysis between ionospheric scintillation levels and receiver tracking performance. *Space Weather* **2012**, *10*, S06005. [CrossRef]
5. Basu, S.; Groves, K.M.; Basu, S.; Sultan, P.J. Specification and forecasting of scintillations in communication/navigation links: Current status and future plans. *J. Atmos. Sol. Terr. Phys.* **2002**, *64*, 1745–1754. [CrossRef]
6. Kelley, M.C.; Haerendel, G.; Kappler, H.; Valenzuela, A.; Balsley, B.B.; Carter, D.A.; Ecklund, W.L.; Carlson, C.W.; Häusler, B.; Torbert, R. Evidence for a Rayleigh-Taylor type instability and upwelling of depleted density regions during equatorial spread F. *Geophys. Res. Lett.* **1976**, *3*, 448–450. [CrossRef]
7. Kil, H.; Paxton, L.J.; Jee, G.; Nikoukar, R. Plasma Blobs Associated With Medium-Scale Traveling Ionospheric Disturbances. *Geophys. Res. Lett.* **2019**, *46*, 3575–3581. [CrossRef]
8. Yang, Z.; Liu, Z. Low-Latitude Ionospheric Density Irregularities and Associated Scintillations Investigated by Combining COSMIC RO and Ground-Based Global Positioning System Observations Over a Solar Active Period. *J. Geophys. Res. Space Phys.* **2018**, *123*, 3998–4014. [CrossRef]

9. Liu, Y.; Zhou, C.; Xu, T.; Tang, Q.; Deng, Z.; Chen, G.; Wang, Z. Review of ionospheric irregularities and ionospheric electrodynamic coupling in the middle latitude region. *Earth Planet. Phys.* **2021**, *5*, 462–482. [CrossRef]
10. Perkins, F. SpreadFand ionospheric currents. *J. Geophys. Res.* **1973**, *78*, 218–226. [CrossRef]
11. Watson, C.; Pedatella, N.M. Climatology and Characteristics of Medium-Scale F Region Ionospheric Plasma Irregularities Observed by COSMIC Radio Occultation Receivers. *J. Geophys. Res. Space Phys.* **2018**, *123*, 8610–8630. [CrossRef]
12. Zhong, J.; Lei, J.; Yue, X.; Luan, X.; Dou, X. Middle-Latitudinal Band Structure Observed in the Nighttime Ionosphere. *J. Geophys. Res. Space Phys.* **2019**, *124*, 5857–5873. [CrossRef]
13. Li, G.; Ning, B.; Otsuka, Y.; Abdu, M.A.; Abadi, P.; Liu, Z.; Spogli, L.; Wan, W. Challenges to Equatorial Plasma Bubble and Ionospheric Scintillation Short-Term Forecasting and Future Aspects in East and Southeast Asia. *Surv. Geophys.* **2020**, *42*, 201–238. [CrossRef]
14. Su, S.Y.; Liu, C.H.; Ho, H.H.; Chao, C.K. Distribution characteristics of topside ionospheric density irregularities: Equatorial versus midlatitude regions. *J. Geophys. Res.* **2006**, *111*, A06305. [CrossRef]
15. Zakharenkova, I.; Astafyeva, E. Topside ionospheric irregularities as seen from multisatellite observations. *J. Geophys. Res. Space Phys.* **2015**, *120*, 807–824. [CrossRef]
16. Aol, S.; Buchert, S.; Jurua, E. Traits of sub-kilometre F-region irregularities as seen with the Swarm satellites. *Ann. Geophys.* **2020**, *38*, 243–261. [CrossRef]
17. Zakharenkova, I.; Astafyeva, E.; Cherniak, I. GPS and in situ Swarm observations of the equatorial plasma density irregularities in the topside ionosphere. *Earth Planets Space* **2016**, *68*, 120. [CrossRef]
18. Yue, X.; Schreiner, W.S.; Kuo, Y.-H.; Hunt, D.C.; Wang, W.; Solomon, S.C.; Burns, A.G.; Bilitza, D.; Liu, J.-Y.; Wan, W.; et al. Global 3-D ionospheric electron density reanalysis based on multisource data assimilation. *J. Geophys. Res. Space Phys.* **2012**, *117*, A09325. [CrossRef]
19. Zhong, J.; Lei, J.; Wang, W.; Burns, A.G.; Yue, X.; Dou, X. Longitudinal variations of topside ionospheric and plasmaspheric TEC. *J. Geophys. Res. Space Phys.* **2017**, *122*, 6737–6760. [CrossRef]
20. Jin, Y.; Xiong, C.; Clausen, L.; Spicher, A.; Kotova, D.; Brask, S.; Kervalishvili, G.; Stolle, C.; Miloch, W. Ionospheric Plasma Irregularities Based on In Situ Measurements From the Swarm Satellites. *J. Geophys. Res. Space Phys.* **2020**, *125*, e2020JA028103. [CrossRef]
21. Jin, Y.; Spicher, A.; Xiong, C.; Clausen, L.B.N.; Kervalishvili, G.; Stolle, C.; Miloch, W.J. Ionospheric Plasma Irregularities Characterized by the Swarm Satellites: Statistics at High Latitudes. *J. Geophys. Res. Space Phys.* **2019**, *124*, 1262–1282. [CrossRef]
22. Pi, X.; Mannucci, A.J.; Lindqwister, U.J.; Ho, C.M. Monitoring of global ionospheric irregularities using the Worldwide GPS Network. *Geophys. Res. Lett.* **1997**, *24*, 2283–2286. [CrossRef]
23. Burke, W.J.; Huang, C.Y.; Gentile, L.C.; Bauer, L. Seasonal-longitudinal variability of equatorial plasma bubbles. *Ann. Geophys.* **2004**, *22*, 3089–3098. [CrossRef]
24. Xiong, C.; Park, J.; Lühr, H.; Stolle, C.; Ma, S.Y. Comparing plasma bubble occurrence rates at CHAMP and GRACE altitudes during high and low solar activity. *Ann. Geophys.* **2010**, *28*, 1647–1658. [CrossRef]
25. Huang, C.-S.; de La Beaujardiere, O.; Roddy, P.A.; Hunton, D.E.; Liu, J.Y.; Chen, S.P. Occurrence probability and amplitude of equatorial ionospheric irregularities associated with plasma bubbles during low and moderate solar activities (2008–2012). *J. Geophys. Res. Space Phys.* **2014**, *119*, 1186–1199. [CrossRef]
26. Luo, X.; Gu, S.; Lou, Y.; Cai, L.; Liu, Z. Amplitude scintillation index derived from C/N0 measurements released by common geodetic GNSS receivers operating at 1 Hz. *J. Geod.* **2020**, *94*, 27. [CrossRef]
27. Aa, E.; Zou, S.; Liu, S. Statistical Analysis of Equatorial Plasma Irregularities Retrieved From Swarm 2013–2019 Observations. *J. Geophys. Res. Space Phys.* **2020**, *125*, e2019JA027022. [CrossRef]
28. Kil, H.; Paxton, L.J.; Oh, S.-J. Global bubble distribution seen from ROCSAT-1 and its association with the evening prereversal enhancement. *J. Geophys. Res. Space Phys.* **2009**, *114*, A06307. [CrossRef]
29. Wan, X.; Xiong, C.; Rodriguez-Zuluaga, J.; Kervalishvili, G.N.; Stolle, C.; Wang, H. Climatology of the Occurrence Rate and Amplitudes of Local Time Distinguished Equatorial Plasma Depletions Observed by Swarm Satellite. *J. Geophys. Res. Space Phys.* **2018**, *123*, 3014–3026. [CrossRef]
30. Su, S.Y.; Chao, C.K.; Liu, C.H. On monthly/seasonal/longitudinal variations of equatorial irregularity occurrences and their relationship with the postsunset vertical drift velocities. *J. Geophys. Res. Space Phys.* **2008**, *113*, A05307. [CrossRef]
31. Huba, J.D.; Krall, J. Impact of meridional winds on equatorial spreadF: Revisited. *Geophys. Res. Lett.* **2013**, *40*, 1268–1272. [CrossRef]
32. Abdu, M.A. Day-to-day and short-term variabilities in the equatorial plasma bubble/spread F irregularity seeding and development. *Prog. Earth Planet. Sci.* **2019**, *6*, 11. [CrossRef]
33. Chen, C.H.; Huba, J.D.; Saito, A.; Lin, C.H.; Liu, J.Y. Theoretical study of the ionospheric Weddell Sea Anomaly using SAMI2. *J. Geophys. Res. Space Phys.* **2011**, *116*, A04305. [CrossRef]
34. Liu, H.; Pedatella, N.; Hocke, K. Medium-scale gravity wave activity in the bottomside F region in tropical regions. *Geophys. Res. Lett.* **2017**, *44*, 7099–7105. [CrossRef]
35. Shiokawa, K. Statistical study of nighttime medium-scale traveling ionospheric disturbances using midlatitude airglow images. *J. Geophys. Res.* **2003**, *108*, 1052. [CrossRef]

36. Eccles, J.V.; Maurice, J.P.S.; Schunk, R.W. Mechanisms underlying the prereversal enhancement of the vertical plasma drift in the low-latitude ionosphere. *J. Geophys. Res. Space Phys.* **2015**, *120*, 4950–4970. [CrossRef]
37. Yizengaw, E.; Retterer, J.; Pacheco, E.E.; Roddy, P.; Groves, K.; Caton, R.; Baki, P. Postmidnight bubbles and scintillations in the quiet-time June solstice. *Geophys. Res. Lett.* **2013**, *40*, 5592–5597. [CrossRef]
38. Huang, C.-S.; Kelley, M.C. Nonlinear evolution of equatorial spreadF: 1. On the role of plasma instabilities and spatial resonance associated with gravity wave seeding. *J. Geophys. Res. Space Phys.* **1996**, *101*, 283–292. [CrossRef]
39. Otsuka, Y. Review of the generation mechanisms of post-midnight irregularities in the equatorial and low-latitude ionosphere. *Prog. Earth Planet. Sci.* **2018**, *5*, 57. [CrossRef]
40. Miller, E.S.; Makela, J.J.; Kelley, M.C. Seeding of equatorial plasma depletions by polarization electric fields from middle latitudes: Experimental evidence. *Geophys. Res. Lett.* **2009**, *36*, L18105. [CrossRef]
41. Otsuka, Y.; Ogawa, T.; Effendy. VHF radar observations of nighttime F-region field-aligned irregularities over Kototabang, Indonesia. *Earth Planets Space* **2009**, *61*, 431–437. [CrossRef]
42. Wan, X.; Xiong, C.; Wang, H.; Zhang, K.; Yin, F. Spatial Characteristics on the Occurrence of the Nighttime Midlatitude Medium-Scale Traveling Ionospheric Disturbance at Topside Ionosphere Revealed by the Swarm Satellite. *J. Geophys. Res. Space Phys.* **2020**, *125*, e2019JA02773. [CrossRef]
43. Zhang, Y.; Wu, J.; Guo, L.; Hu, Y.; Zhao, H.; Xu, T. Influence of solar and geomagnetic activity on sporadic-E layer over low, mid and high latitude stations. *Adv. Space Res.* **2015**, *55*, 1366–1371. [CrossRef]
44. Kelley, M.C. Case studies of coupling between the E and F regions during unstable sporadic-Econditions. *J. Geophys. Res.* **2003**, *108*, 1447. [CrossRef]
45. Park, J.; Lühr, H.; Min, K.W.; Lee, J.-J. Plasma density undulations in the nighttime mid-latitude F-region as observed by CHAMP, KOMPSAT-1, and DMSP F15. *J. Atmos. Sol. Terr. Phys.* **2010**, *72*, 183–192. [CrossRef]